First-principles Simulation of Piezoresistivity
of Transition Metal Dichalcogenide Monolayers

Koichi Nakamura[1,2*]

[1]Center for the Promotion of Interdisciplinary Education and Research, Kyoto University,
Kyoto 615-8540, Japan
[2]Department of Materials Science and Engineering, Egypt-Japan University of Science and Technology,
New Borg El-Arab, Alexandria 21934, Egypt

Longitudinal gauge factors of transition metal dichalcogenide (TMDC) monolayer models have been evaluated by first-principles calculation. TMDC monolayers have a multivalley/multipeak electronic structure, and uniaxial tensile strain causes a significant change in electrical conductivity through carrier redistribution in conduction-band valleys or valence-band peaks for some species of doped TMDC monolayers. A high piezoresistivity was observed selectively depending on the combination of transition metal and chalcogen atoms. In this simulation, a p-doped MoS_2 monolayer model gave high longitudinal gauge factors of 94.2 and 87.4 at 20 °C in the carrier concentration range of 10^{17}–10^{19} cm^{-3}.

1. Introduction

The exploration of novel high-sensitivity piezoresistive materials is indispensable for expanding the usability and operability of force-sensing micro/nano-electromechanical system (MEMS/NEMS) devices. Transition metal dichalcogenide (TMDC) layers have attracted much attention as new candidates of piezoresistive materials composing MEMS mechanical sensors. In particular, TMDC monolayers containing Group VI transition metals, such as molybdenum (Mo) and tungsten (W), have been the subject of a great deal of interest as a post-graphene two-dimensional nanomaterial for application to MEMS devices in various fields of electronics, photonics, and spintronics.[1–10]

In contrast to graphene, the TMDC is a typical semiconducting material with a clear band gap, and the effective masses of carrier electrons and holes are nonzero.[11–24] From the viewpoint of piezoresistivity, the measurement or evaluation of gauge factors (GFs) of TMDCs is a key issue for future application to mechanical sensors. Recently, the evaluation of GFs of Mo disulfide (MoS_2) with 1–3 layers has been reported by the finite-element method with AFM measurement data.[25] On the other hand, the author has already developed the theory and simulation method to evaluate the piezoresistivity of any semiconducting materials on the basis of first-principles calculation.[26–28] The electronic structures of TMDC monolayers have

*Corresponding author: e-mail: koichi@cpier.kyoto-u.ac.jp

been investigated by many researchers, and the author has also presented the details of band structures of TMDC monolayers for the simulation of thermoelectric properties.[11] It is well known that the electronic structures of TMDC monolayers containing Group VI transition metals are affected significantly by spin-orbit coupling.[11–24] In the analysis of TMDC properties regarding stress or strain such as piezoresistivity, the influence of spin-orbit coupling on stress or strain should be sufficiently incorporated.

In this study, longitudinal GFs in doped TMDC monolayer models MX_2 (M = Mo and W; X = S, Se, and Te) have been simulated in terms of first-principles band structures, and the potential of TMDC monolayers for piezoresistive materials shall be discussed.

2. Details of Simulation Method

2.1 First-principles calculation

The electronic band structures of the TMDC monolayer models have been calculated using the VASP program package[29,30] based on the density functional theory (DFT).[31] For DFT exchange-correlation interaction, the generalized-gradient approximation method was used with the Perdew–Wang (PW91) functional.[32,33] The projector augmented wave (PAW) method was adopted,[34] and the cutoff energy for wave functions of electrons was set at 40 Ry (544 eV). Spin-orbit coupling was included in all DFT calculations. The k-point sampling was set by the Monkhorst–Pack grids[35] of 6 × 6 × 1 for geometry optimization and of 48 × 48 × 1 for carrier integration in the Brillouin zone.

Figure 1 shows unit cells of the TMDC monolayer models in this study. The configuration of Mo and W atoms is trigonal prismatic for MoX_2 and WX_2. For the direction vertical to
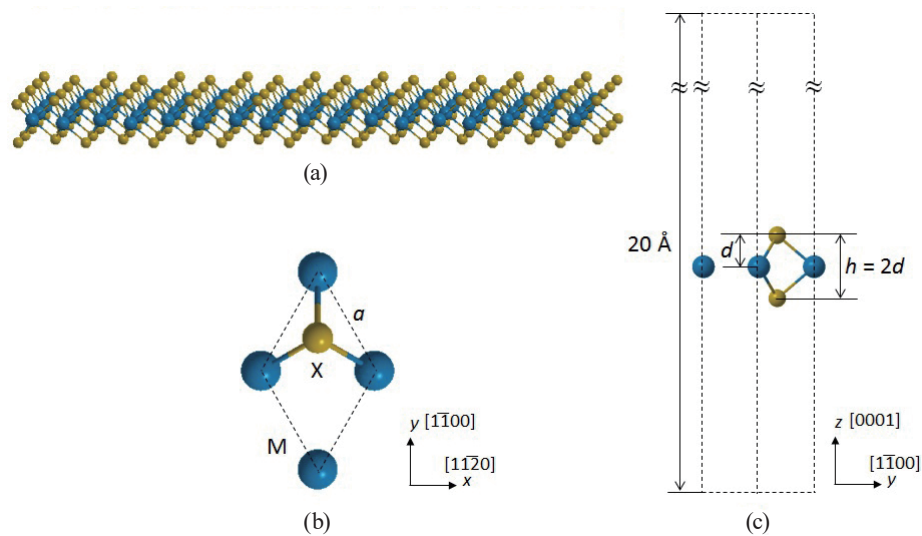

Fig. 1.   (Color online) TMDC models for first-principles calculation (M = Mo and W; X = S, Se, and Te): (a) image of TMDC monolayer and (b) top and (c) side views of unit cell of TMDC monolayer model.

the two-dimensional monolayer, the vacuum space was introduced for establishing a three-dimensional periodic boundary condition by setting the fixed vertical cell parameter to 20 Å. Table 1 shows the optimized geometrical parameters a and d shown in Fig. 1 for the TMDC monolayer models,[11] and the volume per unit cell was defined by $V = \left(\sqrt{3}/2\right)a^2h$, where h is the layer thickness and is conveniently regarded as $2d$ in this study.

The effect of uniaxial tensile strain on the TMDC plane was represented by partial optimization with a fixed scale along the tensile direction. In this study, 1% tensile-strained models were introduced by applying the uniaxial tensile strain $\varepsilon = 0.01$ along the $[11\bar{2}0]$ and $[1\bar{1}00]$ directions. As reported by Yu *et al.*,[36] Poisson's ratios were obtained as negative values, ranging from −0.02 to −0.10, for all TMDC monolayer models.

2.2 Evaluation of gauge factor

In the two-dimensional transport model of doped semiconductors with a multivalley and/or multipeak electronic structure, the electrical conductivity tensor G or electrical resistivity tensor ρ can be represented as a 2×2 tensor in terms of carrier densities and effective mass tensors by

$$G = (\rho)^{-1} = e^2 \left[\sum_{j \in \mathrm{CB}} \sum_{\alpha} n_{j,\alpha} \left(m^*_{j,\alpha} \right)^{-1} \tau_{j,\alpha} + \sum_{j \in \mathrm{VB}} \sum_{\beta} n_{j,\beta} \left(m^*_{j,\beta} \right)^{-1} \tau_{j,\beta} \right], \tag{1}$$

where $n_{j,\alpha}$ is the jth conduction-band (CB) carrier electron density for the CB valley α, $p_{j,\beta}$ is the jth valence-band (VB) hole density for the VB peak β, $m^*_{j,\alpha}$, and $m^*_{j,\beta}$ are band effective mass tensors, $\tau_{j,\alpha}$ and $\tau_{j,\beta}$ are relaxation time tensors, and e^2 is the square of the absolute value of the elementary electric charge.[37] An excess or lack of electrons as large as one particle per unit cell, in order to carry out regular first-principles calculation in the n- or p-doped semiconductor state, should lead to an enormous overestimation of carrier concentration. In actual doped TMDC monolayers, the total number of carrier electrons or holes per unit cell, δ, must be less by a few orders than 1. Under the condition that a small amount of carrier occupation causes no significant changes in band structure, δ can be given by an appropriate shift in the Fermi energy E_F as

Table 1
Optimized geometrical parameters for TMDC monolayer models.

X	MoX_2		WX_2	
	a (Å)	d (Å)	a (Å)	d (Å)
Disulfide (S)	3.190	1.561	3.190	1.563
Diselenide (Se)	3.311	1.690	3.312	1.695
Ditelluride (Te)	3.580	1.803	3.580	1.803

$$\delta = \sum_{j \in \text{CB}} \sum_{\alpha} n_{j,\alpha} V = \sum_{j \in \text{CB}} \sum_{k} w_{k} \left[\exp\left(\frac{E_{j,k} - E_F}{k_B T} \right) + 1 \right]^{-1} , \qquad (2)$$

$$\delta = \sum_{j \in \text{VB}} \sum_{\beta} p_{j,\beta} V = \sum_{j \in \text{VB}} \sum_{k} w_{k} \left[\exp\left(-\frac{E_{j,k} - E_F}{k_B T} \right) + 1 \right]^{-1} , \qquad (3)$$

in the n- or p-type carrier occupation with the temperature T, respectively, where $E_{j,k}$ is the intrinsic-semiconductor-state band energy of the jth subband at the k point, w_k is the k-point weight for k, and k_B is the Boltzmann constant. Practically, $\delta = NV$ was set to an appropriate constant that corresponds to the carrier concentration N ranging from 1×10^{17} to 1×10^{19} cm^{-3}, and then E_F was solved according to Eq. (2) or (3). The values of $n_{j,\alpha}$ and $p_{j,\beta}$ were respectively determined by regional partitioning as

$$n_{j,\alpha} = \sum_{k \in R_\alpha} w_{k} \left[\exp\left(\frac{E_{j,k} - E_F}{k_B T} \right) + 1 \right]^{-1} / V , \qquad (4)$$

$$p_{j,\beta} = \sum_{k \in R_\beta} w_{k} \left[\exp\left(-\frac{E_{j,k} - E_F}{k_B T} \right) + 1 \right]^{-1} / V , \qquad (5)$$

where R_α is the region of the CB valley α and R_β is the region of the VB peak β.[26]

The band effective mass tensors in each region can be defined as 2×2 tensors,

$$\left(m_{j,\gamma}^{*} \right)^{-1} = \pm \frac{1}{\hbar^2} R \begin{pmatrix} \partial^2 E_j / \partial k_x^2 & \partial^2 E_j / \partial k_x \partial k_y \\ \partial^2 E_j / \partial k_y \partial k_x & \partial^2 E_j / \partial k_y^2 \end{pmatrix} R^{\text{T}} , \qquad (6)$$

at the minimum band energy E_j in R_α or the maximum E_j in R_β. $\hbar$ is equal to Planck's constant divided by 2π and R is the planar rotation matrix around the $k_z \parallel [0001]$ axis. On the right-hand side in Eq. (6), a positive sign is adopted for carrier electrons ($\gamma = \alpha$) and a negative sign for holes ($\gamma = \beta$). In this paper, the x- and y-directions can be respectively defined as the $[11\bar{2}0]$ and $[1\bar{1}00]$ directions, and R becomes a unit matrix in this definition. For the relaxation times, we have adopted the approximation that all of the band relaxation times are equal and constant regardless of strain,[26–28] because the variation rate of carrier conductivity can be easily and adequately represented by cancelling most of the band relaxation times.

Under the uniaxial tensile strain ε, the longitudinal GF K_l is defined as

$$K_l = \Delta \rho_l / \rho_l^0 \varepsilon , \qquad (7)$$

where $\rho_l{}^0$ is the longitudinal diagonal element of the resistivity tensor $\boldsymbol{\rho}$ without strain and $\Delta\rho_l$ is the variation in resistivity in the direction toward the uniaxial tensile strain.

3.   Results and Discussion

3.1   Carrier redistribution by uniaxial strain

The details of the multivalley/multipeak band structure for the TMDC monolayer models have been reported in the author's previous study.[11] The band diagrams in the vicinities of the CB bottom and VB top for each TMDC monolayer model are shown in Fig. 2. For the CB bottom of monolayers, there are deep valleys not only at the K points but at the ΓK points along the Γ–K paths. Valleys at the ΓM points along the Γ–M paths are actually very shallow for the direction perpendicular to the Γ–M paths toward the ΓK valleys, so the occupation of carrier electrons on the ΓM valleys can be ignored. For the VB top, there are peaks at the K and Γ points. Figure 3 shows the regional partitioning to define R_α (R_K, $R_{\Gamma K1}$, and $R_{\Gamma K2}$) and R_β (R_K and R_Γ) for computing $n_{j,\alpha}$ and $p_{j,\beta}$ for each valley or peak for Eqs. (4) and (5). Six K valleys and six K peaks on the corners of the Brillouin zone respectively remain equivalent with the application of any strain,[27] and they can be treated as one valley and one peak. On the other hand, the uniaxial strain gives a small difference in band energy level among six ΓK valleys. By applying the uniaxial strain in the [11$\bar{2}$0] and [1$\bar{1}$00] directions, six ΓK valleys are split into four ΓK$_1$ valleys and two ΓK$_2$ valleys.
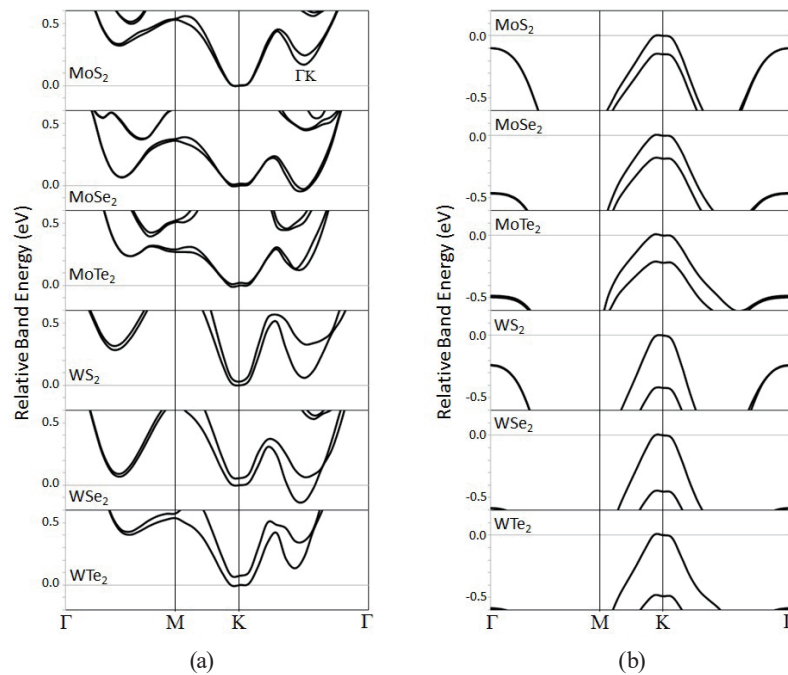

Fig. 2.   Band energy diagrams of the strain-free TMDC monolayer models for (a) CB bottom and (b) VB top. The energy zero is defined by the energy at the K point for CB and VB.
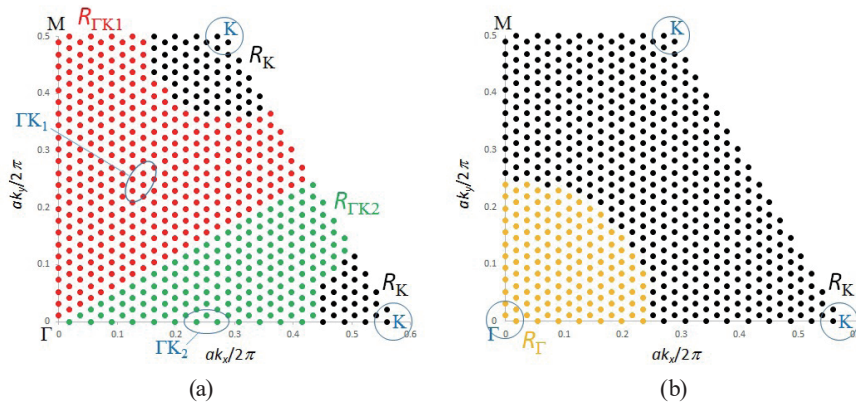
Fig. 3.   (Color online) Regional partitioning of (a) CB bottom and (b) VB top for the range of k_x, $k_y > 0$. Plots are $48 \times 48 \times 1$ Monkhorst–Pack grids for carrier integration.

The temperature dependences of the carrier electron occupation ratios for the strain-free and [11$\bar{2}$0] tensile-strained TMDC monolayer models are shown in Fig. 4. For n-doped MoSe$_2$ and WSe$_2$, carrier electrons are distributed on both the ΓK and K valleys, because the ΓK valleys in MoSe$_2$ lie on almost the same band energy level of the K valleys, and the ΓK valleys clearly lie lower than the K valleys in WSe$_2$ at the calculation level in this paper. By applying the uniaxial strain, a remarkable redistribution of carrier electrons can be easily triggered from the ΓK valleys to the K valleys in both n-doped MoSe$_2$ and WSe$_2$ monolayer models. On the other hand, the redistribution of carrier electrons can hardly be observed in n-doped MoS$_2$, MoTe$_2$, WS$_2$, and WSe$_2$. The changes in carrier electron occupation ratio by the tensile strain for MoSe$_2$ and WSe$_2$ models can be supported by the band energy diagram for the corresponding tensile-strained models shown in Fig. 5. The relative band energy levels at the ΓK$_1$ and ΓK$_2$ valleys to the K valley are raised by 0.05 and 0.03 eV for MoSe$_2$ and WSe$_2$, respectively, owing to the 1% tensile strains.

For the VB of monolayer models, all holes are located at the K point in p-doped TMDCs except for MoS$_2$, and the redistribution of holes cannot occur in the presence of any strain. Only in the MoS$_2$ model, the band energy of the Γ peak is close to that of the K peak, and holes are distributed on both the K and Γ peaks for p-doped MoS$_2$. Figure 6 shows the temperature dependences of the hole occupation ratios for the strain-free and [11$\bar{2}$0] tensile-strained monolayer models. The uniaxial strain can give rise to the redistribution of holes from the K point to the Γ point. The change in hole occupation ratio by the tensile strain for the MoS$_2$ model can also be supported by the band energy diagram for the corresponding tensile-strained models shown in Fig. 7. The difference in band energy level between the Γ and K peaks is clearly reduced by 0.06–0.07 eV for MoS$_2$ owing to the 1% tensile strains. The carrier occupation ratios shown in Figs. 4 and 6 are almost independent of carrier concentration in the range of 10^{17}–10^{19} cm^{-3} for all TMDC models. The [1$\bar{1}$00] tensile strain gives almost the same effect as the [11$\bar{2}$0] tensile strain on the carrier occupation ratio except for the ΓK$_1$ and ΓK$_2$ valleys.
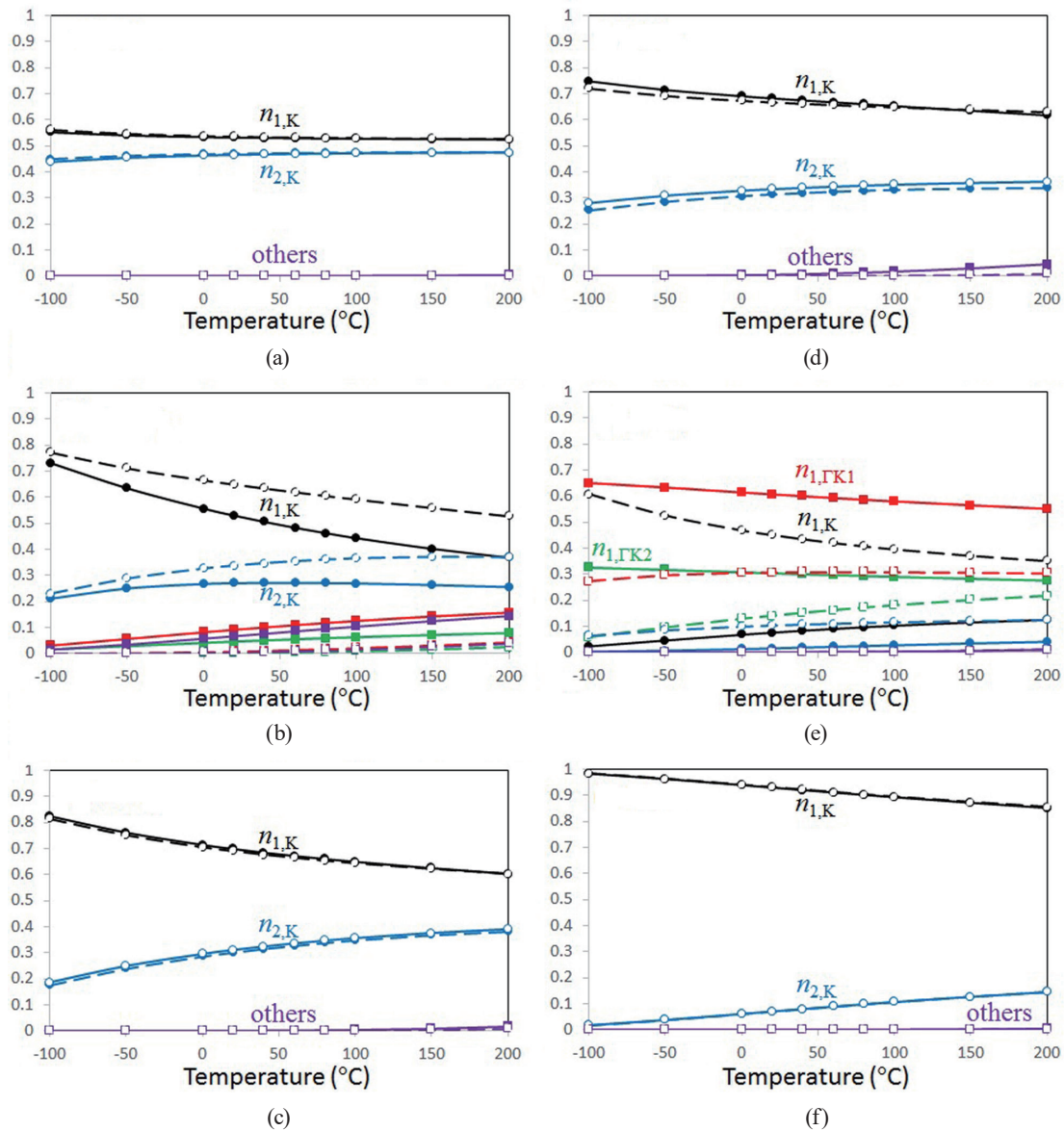
Fig. 4.   (Color online) Temperature dependences of the carrier electron occupation ratios for the n-doped strain-free and [$11\bar{2}0$] tensile-strained TMDC monolayer models at 10^{18} cm^{-3} carrier concentration: (a) MoS$_2$, (b) MoSe$_2$, (c) MoTe$_2$, (d) WS$_2$, (e) WSe$_2$, and (f) WTe$_2$. The black, blue, red, and green curves correspond to $n_{1,K}$, $n_{2,K}$, $n_{1,\Gamma K1}$, and $n_{1,\Gamma K2}$, respectively, for the *j*th lowest CB subbands in unit of δ/V. The solid lines and filled marks are for the strain-free models, whereas the dashed line and open marks are for the [$11\bar{2}0$] tensile-strained models.

3.2   Longitudinal GFs

The calculated longitudinal GFs of the doped TMDC monolayer models are shown in Table 2. The carrier concentration dependence of GFs was hardly observed in the carrier concentration range of 10^{17}–10^{19} cm^{-3}, and the calculated GFs show a similar tendency between the [$11\bar{2}0$] and [$1\bar{1}00$] directions for all TMDC monolayer models. The effective masses in these TMDC
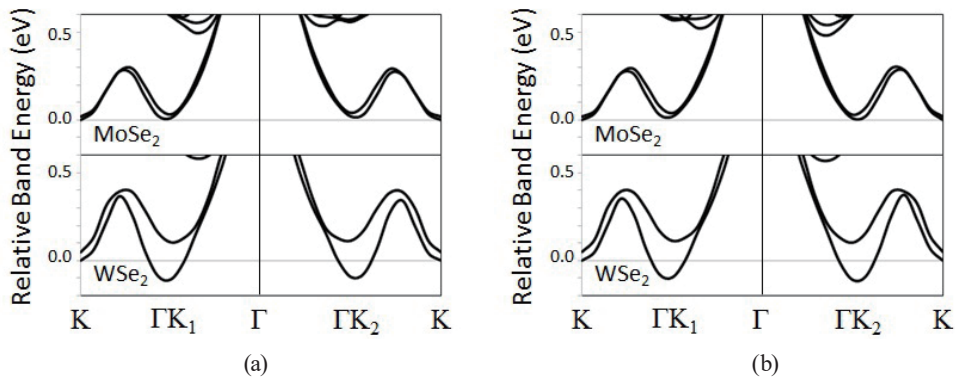
Fig. 5.   Band energy diagrams of the (a) [$1\bar{1}00$] and (b) [$11\bar{2}0$] tensile-strained TMDC monolayer models for CB bottom. The energy zero is defined by the energy at the K point for CB.
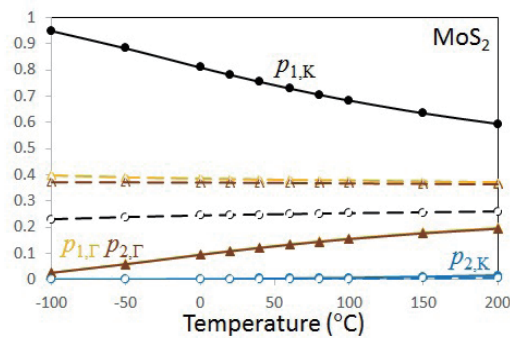

Fig. 6.   (Color online) Temperature dependences of the hole occupation ratios for the p-doped strain-free and [$11\bar{2}0$] tensile-strained MoS$_2$ monolayer models at 10^{18} cm^{-3} carrier concentration. The black, blue, orange, and brown curves correspond to $p_{1,\mathrm{K}}$, $p_{2,\mathrm{K}}$, $p_{1,\Gamma}$, and $p_{2,\Gamma}$, respectively, for the jth highest VB subbands in unit of δ/V. The solid lines and filled marks are for the strain-free models, whereas the dashed line and open marks are for the [$11\bar{2}0$] tensile-strained models.
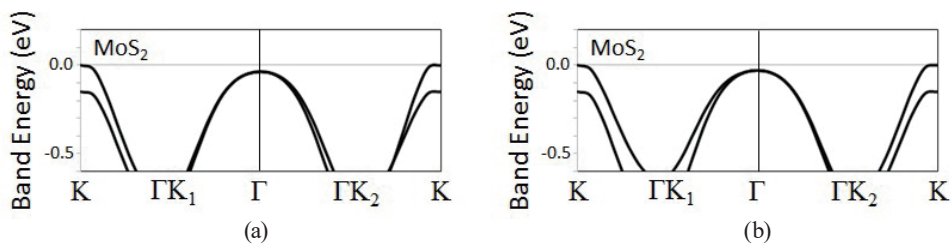

Fig. 7.   Band energy diagrams of the (a) [$1\bar{1}00$] and (b) [$11\bar{2}0$] tensile-strained TMDC monolayer models for VB top. The energy zero is defined by the energy at the K point for VB.

models are hardly affected by uniaxial strain or stress, so the piezoresistivity arises mainly from the carrier redistribution. An effect of the intervalley scattering is small enough to neglect for the models with the effective carrier redistribution. For the models where uniaxial strain or stress does not cause the carrier redistribution, the GFs are very small. As discussed above, the

Table 2
Calculated longitudinal GFs of TMDC monolayer models at 20 °C.

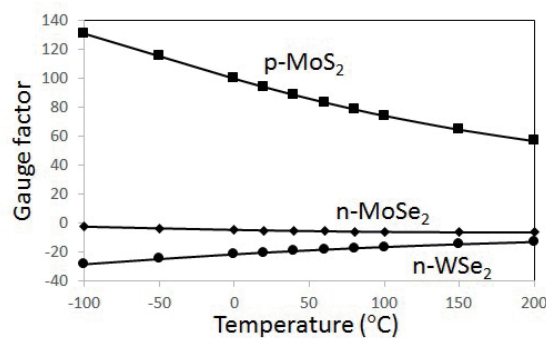| TMDC	n-doped (10^{18} cm^{-3})		p-doped (10^{18} cm^{-3})	
monolayer	[$11\bar{2}0$] direction	[$1\bar{1}00$] direction	[$11\bar{2}0$] direction	[$1\bar{1}00$] direction
MoS$_2$	−0.8	0.1	94.2	87.4
MoSe$_2$	−8.7	−5.7	2.7	3.2
MoTe$_2$	0.1	0.7	2.3	2.5
WS$_2$	−0.1	0.8	3.4	3.8
WSe$_2$	−20.6	−16.4	2.5	2.8
WTe$_2$	2.2	3.2	1.9	2.2

Fig. 8.   Temperature dependence of longitudinal GFs of n-MoSe$_2$, n-WSe$_2$, and p-MoS$_2$ monolayer models in 10^{18} cm^{-3} carrier concentration. All plots are averaged values of GFs for [$1\bar{1}00$] and [$11\bar{2}0$] directions.

effective carrier redistribution can be observed in n-doped MoSe$_2$ and WSe$_2$ and p-doped MoS$_2$ monolayer models, and then significant GFs are obtained in these models. In particular, the p-doped MoS$_2$ monolayer model gives high longitudinal GFs, namely, 94.2 and 87.4 for the [$11\bar{2}0$] and [$1\bar{1}00$] directions, respectively.

However, the GFs in n-doped MoSe$_2$ and WSe$_2$ models are not very high, because the effective masses at the K valleys are not far from those at the ΓK valleys. In contrast, the diagonal elements of the reciprocal effective-mass tensor in Eq. (6) at the Γ peaks are 0.21–0.33 times as much as those at the K peaks for the MoS$_2$ monolayer model, and therefore, a drastic decrease in electric conductivity should be observed by the hole transfer from the K peaks to the Γ point.

For each of n-doped MoSe$_2$ and WSe$_2$ and p-doped MoS$_2$ monolayer models, the longitudinal GF for the [$11\bar{2}0$] direction is slightly larger than that for the [$1\bar{1}00$] directions. This crystal anisotropy in GF is due to a tiny difference in the amount of carrier redistribution in the first-principles calculation. As discussed above, the mechanisms of the longitudinal piezoresistance effect in n-doped MoSe$_2$ and WSe$_2$ and p-doped MoS$_2$ monolayer models are common for the [$11\bar{2}0$] and [$1\bar{1}00$] directions; therefore, it can be regarded that the crystal anisotropy in piezoresistance should be small. The temperature dependence of longitudinal GFs in specific models is shown in Fig. 8. Similarly to general semiconducting materials, the absolute values of longitudinal GFs decrease as temperature increases.

4.   Conclusions

The longitudinal GFs of MX_2 TMDC monolayer models (M = Mo and W; X = S, Se, and Te) have been evaluated by first-principles calculation. TMDC monolayers have a multivalley/multipeak electronic structure, and effective regional partitioning for carrier redistribution has been presented. For some species of doped TMDC monolayers, uniaxial tensile strain causes a significant change in electrical conductivity through carrier redistribution in CB valleys or VB peaks. A high piezoresistivity was observed selectively depending on the combination of M and X. In this simulation, a p-doped MoS_2 monolayer model gave high longitudinal GFs of 94.2 for the $[11\bar{2}0]$ direction and 87.4 for the $[1\bar{1}00]$ direction at 20 °C in the carrier concentration range of 10^{17}–10^{19} cm^{-3}, based on the hole transfer from the K peaks to the Γ point by the uniaxial strain or stress with the change in effective mass.

Acknowledgments

References

1   J. A. Wilson and A. D. Yoffe: Adv. Phys. **18** (1963) 193.
2   A. Splendiani, L. Sun, Y. Zhang, T. Li, J. Kim, C.-Y. Chim, G. Galli, and F. Wang: Nano Lett. **10** (2010) 1271.
3   B. Radisavljevic, A. Radenovic, J. Brivio, V. Giacometti, and A. Kis: Nat. Nanotechnol. **6** (2011) 147.
4   H. Zeng, J. Dai, W. Yao, D. Xiao, and X. Cui: Nat. Nanotechnol. **7** (2012) 490.
5   K. F. Mak, K. He, J. Shan, and T. F. Heinz: Nat. Nanotechnol. **7** (2012) 494.
6   Q. H. Wang, K. Kalantar-Zadeh, A. Kis, J. N. Coleman, and M. S. Strano: Nat. Nanotechnol. **7** (2012) 699.
7   Y. Chen, J. Xi, D. O. Dumcenco, Z. Liu, K. Suenaga, D. Wang, Z. Shuai, Y.-S. Huang, and L. Xie: ACS Nano **7** (2013) 4610.
8   R. S. Sundaram, M. Engel, A. Lombardo, R. Krupke, A. C. Ferrari, Ph. Avouris, and M. Steiner: Nano Lett. **13** (2013) 1416.
9   O. Lopez-Sanchez, D. Lembke, M. Kayci, A. Radenovic, and A. Kis: Nat. Nanotechnol. **8** (2013) 497.
10   S. B. Desai, S. R. Madhvapathy, A. B. Sachid, J. P. Llinas, Q. Wang, G. H. Ahn, G. Pitner, M. J. Kim, J. Bokor, C. Hu, H.-S. P. Wong, and A. Javey: Science **354** (2016) 99.
11   K. Nakamura: Jpn. J. Appl. Phys. **57** (2018) 06HE04.
12   L. F. Mattheiss: Phys. Rev. B **8** (1973) 3719.
13   A. Kuc, N. Zibouche, and Y. Heine: Phys. Rev. B **83** (2011) 245213.
14   Z. Y. Zhu, Y. C. Cheng, and U. Schwingenschlögl: Phys. Rev. B **84** (2011) 153402.
15   T. Cao, G. Wang, W. Han, H. Ye, C. Zhu, J. Shi, Q. Niu, P. Tan, E. Wang, B. Liu, and J. Feng: Nat. Commun. **3** (2012) 887.
16   D. Xiao, G.-B. Liu, W. Feng, X. Xu, and W. Yao: Phys. Rev. Lett. **108** (2012) 196802.
17   A. Kumar and P. K. Ahluwalla: Eur. Phys. J. B **85** (2012) 186.
18   A. Ramasubramaniam: Phys. Rev. B **86** (2012)115409.
19   C. Gong, H. Zhang, W. Wang, L. Colobmo, R. M. Wallace, and K. Cho: Appl. Phys. Lett. **103** (2013) 053513.
20   H.-P. Komsa and A. V. Krasheninnikov: Phys. Rev. B **88** (2013) 085318.
21   G.-B. Liu, W.-Y. Shan, Y. Yao, W. Yao, and D. Xiao: Phys. Rev. B **88** (2013) 085433.
22   K. Kośmider, J. W. González, and J. Fernández-Rossier: Phys. Rev. B **88** (2013) 245436.
23   X Xu, W. Yao, D. Xiao, and T. F. Heinz: Nat. Phys. **10** (2014) 343.
24   J. A. Reyes-Retana and F. Cervantes-Sodi: Sci. Rep. **6** (2016) 24093.
25   S. Manzeli, A. Allain, A. Ghadimi, and A. Kis: Nano Lett. **15** (2015) 5330.

26   K. Nakamura, Y. Isono, T. Toriyama, and S. Sugiyama: Phys. Rev. B **80** (2009) 045205.
27   K. Nakamura, T. Toriyama, and S. Sugiyama: J. Appl. Phys. **50** (2011) 06GE05.
28   K. Nakamura, Y. Isono, and T. Toriyama: Jpn. J. Appl. Phys. **47** (2008) 5132.
29   G. Kresse and J. Hafner: Phys. Rev. B **47** (1993) R558.
30   G. Kresse and J. Furthmüller: Phys. Rev. B **54** (1996) 11169.
31   P. Hohenberg and W. Kohn: Phys. Rev. **136** (1964) B864.
32   J. P. Perdew and Y. Wang: Phys. Rev. B **45** (1992) 13244.
33   J. P. Perdew, J. A. Chevary, S. H. Vosko, K. A. Jackson, M. R. Pederson, D. J. Singh, and C. Fiolhais: Phys. Rev. B **46** (1992) 6671.
34   P. E. Blöchl: Phys. Rev. B **50** (1994) 17953.
35   H. J. Monkhorst and J. D. Pack: Phys. Rev. B **13** (1976) 5188.
36   L. Yu, Q. Yan, and A. Ruzsinszky: Nat. Commun. **8** (2017) 15224.
37   C. Kittel: Introduction to Solid State Physics (Wiley, New York, 2005) 8th ed., p. 200.

About the Author

Koichi Nakamura received his B.S., M.S., and Ph.D. degrees in molecular engineering from Kyoto University, Japan in 1994, 1996, and 2000, respectively. From 1999 to 2004, he was an assistant professor and from 2004 to 2006, a senior lecturer at Kyoto University. From 2009 to 2011, he was a chair professor at Ritsumeikan University, Japan. Since 2011, he has been an associate professor at Kyoto University and an adjunct professor at Egypt-Japan University of Science and Technology, Egypt. His research interests are in quantum physics and chemistry in materials science and engineering. (koichi@cpier.kyoto-u.ac.jp)